ELSEVIER

Earth and Planetary Science Letters 160 (1998) 505–519

EPSL

Uranium and thorium diffusion in diopside

James A. Van Orman [a,*], Timothy L. Grove [a], Nobumichi Shimizu [b]

[a] *Department of Earth, Atmospheric, and Planetary Sciences, Massachusetts Institute of Technology, Cambridge, MA 02139, USA*
[b] *Department of Geology and Geophysics, Woods Hole Oceanographic Institution, Woods Hole, MA 02543, USA*

Received 25 August 1997; revised version received 26 March 1998; accepted 6 April 1998

Abstract

This paper presents new experimental data on the tracer diffusion rates of U and Th in diopside at 1 atm and 1150–1300ºC. Diffusion couples were prepared by depositing a thin layer of U–Th oxide onto the polished surface of a natural diopside single crystal, and diffusion profiles were measured by ion microprobe depth profiling. For diffusion parallel to [001] the following Arrhenius relations were obtained: $\log_{10} D_{\mathrm{U}} = (-5.75 \pm 0.98) - (418 \pm 28\,\mathrm{kJ/mol})/2.303RT$ $\log_{10} D_{\mathrm{Th}} = (-7.77 \pm 0.92) - (356 \pm 26\,\mathrm{kJ/mol})/2.303RT$. The diffusion data are used to assess the extent to which equilibrium is obtained during near fractional melting of a high-Ca pyroxene bearing mantle peridotite. We find that the diffusion rates for both elements are slow and that disequilibrium between solid and melt will occur under certain melting conditions. For near-fractional adiabatic decompression melting at ascent rates >3 cm/yr, high-Ca pyroxene will exhibit disequilibrium effects. High-Ca pyroxene will become zoned in U and Th and the melts extracted will be depleted in these incompatible elements relative to melts produced by equilibrium fractional melting. U and Th diffusivities in high-Ca pyroxene are similar, and diffusive fractionation of these elements will be limited. Numerical solutions to a dynamic melting model with diffusion-controlled chemical equilibration indicate that the activity ratio [^{230}Th/^{238}U] in a partial melt of spinel peridotite will be slightly less than 1 for a broad range of melting parameters. This result reinforces the already widely accepted conclusion that melting of spinel peridotite cannot account for ^{230}Th excesses in mid-ocean ridge and ocean island basalts, and that garnet must therefore be present over part of the melting column.

Keywords: diffusion; diopside; pyroxene group; uranium disequilibrium; U-238/Th-230; igneous processes

1. Introduction

Radioactive disequilibrium between ^{238}U and ^{230}Th is widely used to infer the rate and style of melting and melt transport in the mantle [1–8]. Making full use of the ^{238}U–^{230}Th system requires knowing in which minerals and at what depths in the mantle U and Th are fractionated from each other. Clinopyroxene (cpx) and garnet are the principal hosts of U and Th in upper mantle rocks and control the fluxes of these elements during melting. Equilibrium mineral/melt partition coefficients for U and Th between clinopyroxene and basaltic melt are small ($\sim 10^{-3}$ to 10^{-2}) and differ by only about a factor of 2, with U being the more incompatible element [9–13]. The similarity between U and Th partition coefficients implies that clinopyroxene has

* Corresponding author. Fax: +1 (617) 253-7102; E-mail: javanorm@mit.edu

0012-821X/98/$19.00
PII S0012-821X(98)00107-1

little ability to fractionate these elements. Even if significant fractionation were possible it would be in the wrong sense to explain the ^{230}Th excesses observed in nearly all recently erupted mid-ocean ridge basalts (MORB) [14,15]. On the other hand, U and Th partition coefficients between garnet and basaltic melt differ by nearly an order of magnitude [11,16,17], with Th being the more incompatible element. The equilibrium partitioning data, then, appear to require melting in the presence of garnet to explain the excess ^{230}Th in MORB. This is an important conclusion because it requires that melting begins at depths greater than ~75 km, where garnet becomes the stable aluminous phase in peridotite [18,19] or, alternatively, that garnet pyroxenite is an important component of the MORB source [20].

The conclusion that clinopyroxene cannot deliver excess ^{230}Th to the melt is valid if chemical equilibrium between cpx and melt is maintained during melting. If, however, diffusion in clinopyroxene is slow relative to the melting rate, then equilibrium may not be achieved. In this case fractionation between U and Th depends strongly on the relative diffusion rates of these elements [21–23]. A reversal in the effective compatibility order of two elements is possible if the more compatible element diffuses significantly faster than the incompatible element [21]. To produce excess ^{230}Th in the melt by a disequilibrium mechanism would require that (1) U diffuses slowly enough in clinopyroxene that equilibrium between cpx and melt is not achieved, and (2) Th diffuses significantly faster than U. To determine whether disequilibrium melting can influence U and Th partitioning, we performed a series of experiments to measure the diffusion rates of U and Th in diopside in the temperature range 1150–1300°C.

2. Experimental and analytical techniques

2.1. Sample preparation

Diffusion experiments were performed on gem quality natural diopside crystals from the Kunlun Mts., China (American Museum of Natural History samples #100242 and #104501). The crystals were light green, transparent, free of cracks and visible inclusions, and had major element compositions very near pure diopside (Table 1). Each crystal was sectioned perpendicular to the *c* crystallographic axis into slabs ~0.5 mm thick. One side of each slab was polished to 0.06 μm alumina grit and then cut into pieces 1–2 mm on a side. These pieces were cleaned ultrasonically in deionized water and then pre-annealed for 2 days at 1200°C, with oxygen fugacity controlled near the quartz–fayalite–magnetite (QFM) buffer.

Table 1
Kunlun Mts. diopside composition

Oxide	Weight (%)
SiO_2	55.5
TiO_2	0.06
Al_2O_3	0.88
FeO^{tot}	0.55
MgO	18.1
CaO	24.7
Na_2O	0.53
Total	100.3

The diffusion source material was deposited as an aqueous solution onto the polished surface of the diopside. A dilute (0.05 M) nitric acid solution that contained dissolved U, Th, and Al in 1:1:4 molar proportions was prepared from 10,000 μg/ml ICP standard solutions and diluted with purified water to 270 μg U/ml. Approximately 1 μl of this solution was deposited onto the polished surface of the diopside, along with a small amount of methanol to reduce surface tension and allow the solution to spread uniformly over the sample surface. The solution was evaporated in air at 120°C, which left a thin layer of nitrates with concentration $\sim 5 \times 10^{-10}$ mol/mm^2. At the conditions of the diffusion anneal, with f_{O2} at the QFM buffer, the nitrates decompose to Al_2O_3 and nearly stoichiometric $UThO_4$ [24,25]. Because U and Th have the same formal charge in the oxide (+4) that they presumably have in diopside, no further redox reactions are necessary to introduce these elements into the diopside lattice. There was no evidence in any of the experiments that the tracer layer reacted with the diopside. We calculate that less than 0.01% of the U and Th diffused into the diopside crystal during any of the experiments, and thus the tracer layer provided an effectively infinite reservoir of U and Th.

Al was added to the tracer solution as a possible charge-balancing species. However, as discussed below in the Analyses section, we were unable to detect Al diffusion profiles in any of our samples, and it is unclear whether Al was actually transported into the crystal during any of the diffusion anneals.

2.2. Diffusion anneals

Diffusion anneals were performed at constant temperature in open Pt crucibles placed in the hotspot of a Deltech DT31VT vertical gas mixing furnace, with anneal times ranging from 2 to 24 days. Run temperature was attained within approximately 5 minutes after introducing the charge into the furnace and was continuously monitored using a $Pt–Pt_{90}Rh_{10}$ thermocouple calibrated against the melting points of NaCl, Au, and Pd. Fluctuation in temperature over the course of each anneal was generally within ± 2ºC, with the exception of a single experiment (UTh1200b) in which the thermocouple degraded during the anneal; temperature for this experiment was assigned an uncertainty of ± 5ºC. Oxygen fugacity was controlled near the QFM buffer by mixing CO_2 and H_2 gases and was continuously monitored with a solid ZrO_2–CaO electrolyte oxygen sensor calibrated against the Fe–FeO, Ni–NiO, and $Cu–Cu_2O$ buffers. Variation in f_{O2} over the course of each experiment was within ± 0.1 log unit. Experiments were quenched by removing the sample from the furnace and allowing it to cool in air. Heating and cooling times were insignificant compared to the anneal durations, and therefore no attempt was made to account for diffusion during run-up or quenching.

In addition to the diffusion anneals, we performed 'zero-time' experiments in order to evaluate systematic errors associated with analysis of the diffusion profiles. Diffusion couples were prepared as above, taken to 1200ºC and held there for approximately five minutes, then quenched in air.

After quenching, samples were rinsed ultrasonically in deionized water, then ethanol. They were then mounted in epoxy with the diffusion source layer facing up and coated with a thin layer of gold, which provided a conductive surface for ion microprobe depth profiling.

2.3. Analyses

Concentration profiles in the annealed samples were measured using the Cameca IMS 3f ion microprobe at the Woods Hole Oceanographic Institution. A primary beam of O^- ions was focused onto the surface of the sample, producing secondary ions that were continuously analyzed in a mass spectrometer. In this procedure successively deeper layers are sampled as the primary beam sputters through the sample, allowing concentrations to be measured as functions of depth. The primary beam was accelerated under a potential of ~8.2 kV and was focused to a diameter of ~20–30 μm, with beam currents usually in the range 10–20 nA. By analyzing 'zero-time' experiments, we found that optimum resolution was achieved by rastering the primary beam over a square area 150–200 μm on a side and inserting a circular mechanical aperture 68 μm in diameter into the secondary optics. The aperture was centered over the sputtered area so that secondary ions were collected only from the central, flat portion of the pit. This configuration optimized depth resolution and minimized contamination of the diffusion profile with material from the tracer layer. In analyses of 'zero-time' experiments, U and Th counts dropped sharply after penetration of the tracer layer, and fell to background levels at a depth of approximately 40 nm.

Secondary ions were measured in a series of cycles in which electron multiplier counts were collected in sequence on masses ^{27}Al (3 s), ^{44}Ca (5 s), ^{232}Th (15–30 s) and ^{238}U (15–30 s). The ^{44}Ca signal was monitored to determine the position of the interface between the tracer layer and the diopside. ^{44}Ca counts increased sharply after the tracer layer was penetrated, which was usually within the first two or three cycles, and then decreased very gradually due to charging of the sample surface. To correct for the charging effect and for small fluctuations in primary beam intensity, ^{232}Th and ^{238}U counts were normalized to ^{44}Ca, and the ratios $^{232}Th/^{44}Ca$ and $^{238}U/^{44}Ca$ were used in place of raw Th and U counts to model diffusion coefficients.

Aluminum concentration profiles in annealed samples were indistinguishable from those from 'zero-time' experiments: Al counts dropped sharply over the upper 20–30 nm and were nearly constant over the remaining depth interval.

2.4. Analysis 'reversals'

In order to be certain that the ion microprobe depth profiling technique was measuring the true concentration profile in the sample, we devised an analysis 'reversal'. We wanted to determine whether the diffusion profile was contaminated during the analysis by material from the tracer layer. Therefore, we reanalyzed one experiment (UTh1200a) from the reverse direction. The sample was extracted from its epoxy mount and remounted in high-strength thin section epoxy on a glass slide, with the tracer layer facing down. It was then carefully ground to a thickness of ~7 μm. After grinding, the thin section was polished with diamond and alumina pastes (to 0.06 μm alumina) and prepared as described above for SIMS depth profiling. Sputtering began on the polished surface and proceeded through the diopside crystal to the tracer layer. A higher primary beam current (30 nA) and smaller raster area (100 μm × 100 μm) were used for this analysis so that the relatively thick sample could be penetrated in a reasonable time (approximately 10 h). In the discussion below, results of this analysis are referred to as a reversal.

2.5. Depth measurement

The depth of each sputtered pit was measured with a Sloan Dektak 8000 surface-contact profilometer equipped with a 2.5 μm diamond-tipped stylus. Prior to making the depth measurements, the gold coat was removed from the sample by ultrasonic rinsing in a KI solution. At least two orthogonal scans were made for each pit, and in each we considered the mean depth over the central ~70 μm. Pits produced under the same primary beam conditions yielded consistent sputtering rate estimates, confirming that the sputtering rate during each analysis was constant. Although the profilometer is capable of measuring depth to a precision of ~1 nm, the uncertainty in the depth measurement was considerably greater, being controlled primarily by the roughness of the sample surface. In most cases the vertical relief at the bottom of the sputtered pit was between 10 and 40 nm.

2.6. Determination of diffusion coefficients

Diffusion in these experiments is well described by the equation for one-dimensional diffusion in a semi-infinite medium, with constant interface concentration [26]:

$$\frac{C(x,t)-C_0}{C_i-C_0}=\mathrm{erf}\left(\frac{x}{2\sqrt{Dt}}\right) \quad (1)$$

where C is the concentration at depth x after annealing time t, C_0 is the concentration at the interface, C_i is the initial concentration in the diopside crystal (essentially zero for both U and Th), and D is the diffusion coefficient. A typical diffusion profile is shown in Fig. 1a. The first few points in the profile were sometimes high due to contamination from the tracer layer, and these points were disregarded in the fitting procedure. To extract a diffusion coefficient from the data, each profile was linearized by plotting the inverse error function of the left-hand side of Eq. 1 against depth (Fig. 1b). The diffusion coefficient was then calculated from the relation $D = (4m^2t)^{-1}$, where m is the slope of the least-squares line fit to the inverted data. On the inverse error function plot, the data scatter and tail off slightly at the deep end of the profile as the concentration drops toward the detectability limit. We fit only the shallower part of the concentration profile and stopped including points when count rates approached background levels. Small adjustments in the interface concentration, C_0, were made in the fitting procedure to force the line through the origin.

3. Results

3.1. Error analysis

There are two types of uncertainty in our data set, one associated with intra-run variability and the second associated with reproducibility of diffusion coefficients for multiple experiments run at similar conditions. The source of uncertainty in the first is associated with error in measurement of the depth profile. In the second case there is the additional source of systematic error associated with our ability to exactly reproduce the conditions of the experiment.

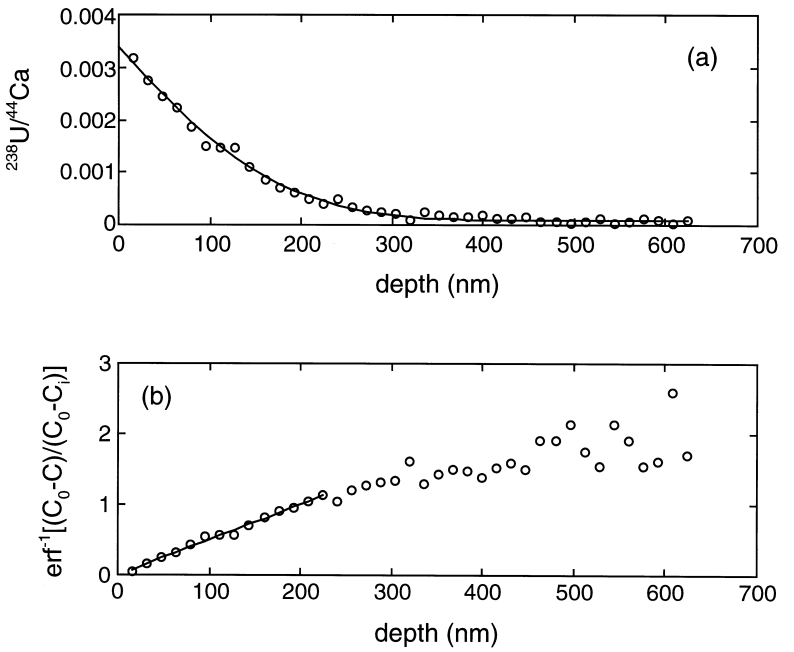

Fig. 1. A typical diffusion profile (a) and its error function inversion (b). The diffusion coefficient is calculated from the slope of the line fit to the inverted data, which is equal to $(2\sqrt{Dt})^{-1}$. The error function curve shown in (a) is a solution to Eq. 1 using the diffusion coefficient calculated from the linear inverse error function fit.

The uncertainties associated with measurement of the diffusion profile can be assessed by comparing diffusion coefficients extracted from individual diffusion profiles from the same experiment. The uncertainty in the reported value of *D* for each profile was estimated from a combination of the error in the crater depth measurement and the formal uncertainty from the linear fit to the erf-inverted diffusion profile. When multiple diffusion profiles were measured on a single sample, these yielded diffusion coefficients that in nearly all cases were identical within error (Table 2). A single diffusion coefficient for each experiment was calculated by taking the weighted average of the results from each diffusion profile, with the weights being equal to the inverse square of the uncertainty in each measurement [27]. These are the uncertainties reported in bold type in Table 2 and shown in the Arrhenius plots in Fig. 4. An independent assessment of the diffusion coefficient measured in the 'forward' profiles is given by our 'reverse' profile measurement. Diffusion coefficients extracted from the reverse concentration profile were in excellent agreement with the forward measurements of the same experiment, and the quality of the profiles was very similar (Fig. 2). A measure of the inter-run reproducibility can be inferred by comparing experiments that were performed under the same temperature conditions. The range of values among duplicate runs is similar to that determined from separate profiles in a single sample (Table 2).

3.2. Time series

If volume diffusion is the mechanism responsible for U and Th transport, then the calculated diffusion coefficients should be independent of the duration of the experiment. We ran three experiments at 1200°C that ranged in duration from 71 to 278 hours (nearly a factor of 4). U and Th diffusion coefficients in these experiments agreed within less than a factor of two (Fig. 3). Two experiments at 1300°C also were in excellent agreement, although they covered a much smaller range in time (56–86 h).

3.3. Temperature dependence of diffusion

The diffusion coefficients calculated for each experiment were used to assess the temperature depen-

Table 2
Run conditions and experimental results

ID	T (°C)	Anneal time (h)	$D_{Th} \pm 1\sigma$ (m^2/s)	$D_U \pm 1\sigma$ (m^2/s)
UTh1150a	1150	576.80	$1.59 \pm 0.31 \times 10^{-21}$	$4.54 \pm 1.55 \times 10^{-22}$
UTh1150b	1150	456.61	$1.18 \pm 0.21 \times 10^{-21}$	$9.52 \pm 1.69 \times 10^{-22}$
			$1.55 \pm 1.09 \times 10^{-21}$	$5.78 \pm 6.98 \times 10^{-22}$
			$\mathbf{1.20 \pm 0.20 \times 10^{-21}}$	$\mathbf{9.44 \pm 1.66 \times 10^{-22}}$
UTh1200a	1200	70.65	$4.56 \pm 1.21 \times 10^{-21}$ [a]	$3.33 \pm 7.27 \times 10^{-21}$ [a]
			$6.38 \pm 2.37 \times 10^{-21}$	$2.54 \pm 1.99 \times 10^{-21}$
			$5.06 \pm 1.00 \times 10^{-21}$	$2.39 \pm 0.70 \times 10^{-21}$
			$6.87 \pm 3.33 \times 10^{-21}$	$4.53 \pm 2.28 \times 10^{-21}$
			$\mathbf{5.26 \pm 0.72 \times 10^{-21}}$	$\mathbf{2.90 \pm 0.69 \times 10^{-21}}$
UTh1200d	1200	199.50	$4.49 \pm 1.05 \times 10^{-21}$	$5.46 \pm 2.10 \times 10^{-21}$
			$2.87 \pm 0.78 \times 10^{-21}$	$2.44 \pm 0.94 \times 10^{-21}$
			$\mathbf{3.80 \pm 0.67 \times 10^{-21}}$	$\mathbf{3.95 \pm 1.08 \times 10^{-21}}$
UTh1200b	1200	277.67	$2.82 \pm 0.94 \times 10^{-21}$	$2.29 \pm 0.82 \times 10^{-21}$
			$3.45 \pm 0.87 \times 10^{-21}$	$2.40 \pm 0.85 \times 10^{-21}$
			$\mathbf{3.22 \pm 0.65 \times 10^{-21}}$	$\mathbf{2.35 \pm 0.59 \times 10^{-21}}$
UTh1	1300	56.22	$1.32 \pm 0.62 \times 10^{-20}$	$1.06 \pm 0.50 \times 10^{-20}$
			$1.39 \pm 0.75 \times 10^{-20}$	$1.84 \pm 0.86 \times 10^{-20}$
			$2.70 \pm 0.83 \times 10^{-20}$	$2.88 \pm 0.74 \times 10^{-20}$
			$\mathbf{2.12 \pm 0.49 \times 10^{-20}}$	$\mathbf{2.35 \pm 0.48 \times 10^{-20}}$
UTh2	1300	86.10	$1.97 \pm 0.81 \times 10^{-20}$	$1.36 \pm 0.69 \times 10^{-20}$
			$3.98 \pm 2.06 \times 10^{-20}$	$3.30 \pm 1.95 \times 10^{-20}$
			$\mathbf{2.75 \pm 0.89 \times 10^{-20}}$	$\mathbf{2.18 \pm 0.84 \times 10^{-20}}$

Values in bold type are weighted averages for each experiment.
[a] This profile was measured in the reverse direction.

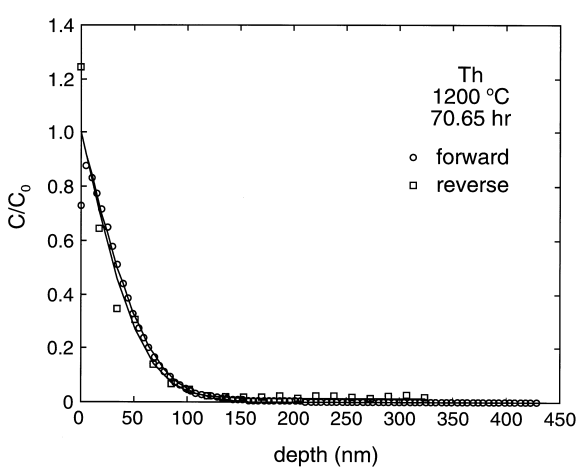

Fig. 2. Comparison of diffusion profiles measured from opposite directions on the same sample. The circles represent a concentration profile measured in the 'forward' direction, through the surface diffusant layer. The squares represent a depth profile made in the reverse direction.

dence of U and Th diffusion, which can be described by the Arrhenius equation:

$$D = D_0 e^{-H_a/RT} \quad (2)$$

where D_0 is a frequency factor, H_a is the activation enthalpy, R is the gas constant and T is absolute temperature. Both U and Th show good Arrhenian behavior, exhibiting linear trends on a plot of $\log D$ vs. inverse temperature (Fig. 4). Linear least-squares regressions of the data [28] yield the following Arrhenius relations:

$$\log D_U = (-5.75 \pm 0.98) - (418 \pm 28\,\mathrm{kJ/mol})/2.303RT \quad (3)$$

$$\log D_{Th} = (-7.77 \pm 0.92) - (356 \pm 26\,\mathrm{kJ/mol})/2.303RT \quad (4)$$

where the diffusion coefficients are in units of m^2/s and the uncertainties quoted are $\pm 1\sigma$. Uranium and

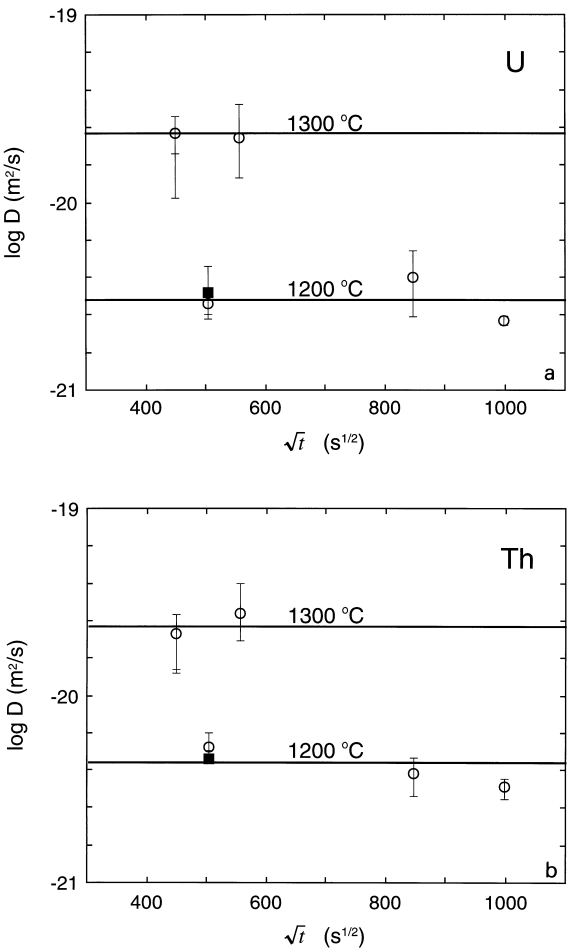

Fig. 3. Time series at 1200°C and 1300°C for U and Th diffusion anneals. The horizontal dashes represent individual measurements of a single experiment, and circles indicate the weighted average. Squares indicate diffusion coefficients extracted from 'reverse' profiles.

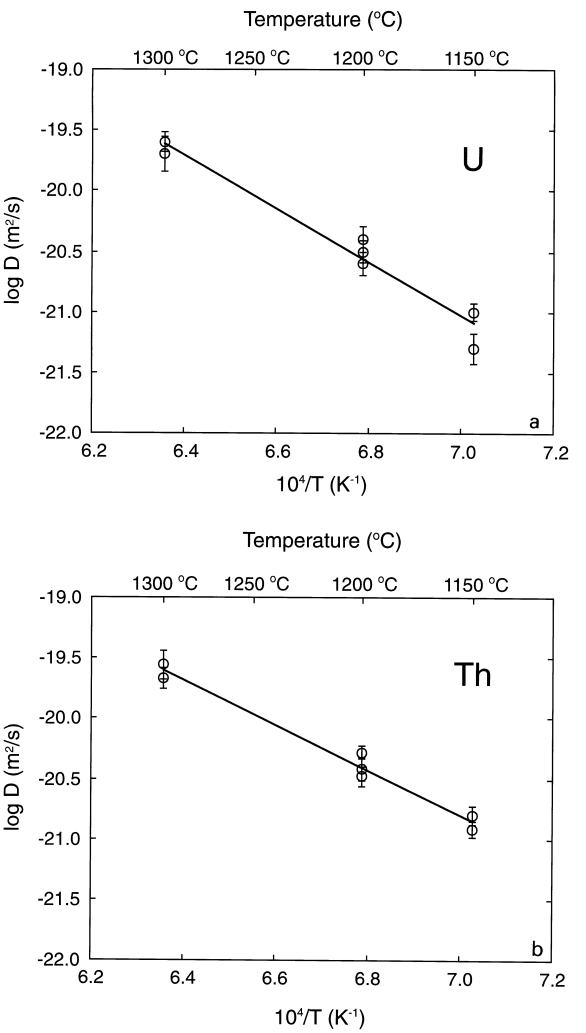

Fig. 4. Arrhenius plots of U and Th diffusivity between 1150 and 1300°C. The circles represent average diffusion coefficients for each experiment, and the solid lines are weighted least-squares fits to the data. Activation enthalpies and pre-exponential factors are given in the text.

thorium diffusivities converge with increasing temperature and are very similar near the melting point of diopside.

4. Discussion

4.1. Comparison with other diffusion data in diopside

Seitz [29] reported a U tracer diffusion coefficient for diopside of 10^{-16} m^2/s at 1240°C, which is four orders of magnitude higher than our results for U diffusion. His experiments involved diopside crystals annealed in a diopside–albite–anorthite melt, and it is possible that growth of the crystals during the experiment accounts for the high apparent diffusivity.

Experimental measurements of tracer-, self-, and inter-diffusion coefficients have been reported for several other cations in natural diopside, and these are in good general agreement with our results

(Fig. 5). The tracer diffusion data for cations that partition onto the M2 site are broadly consistent with trends observed in other minerals: diffusion rates increase with decreasing ionic charge and with decreasing ionic radius. The influence of ionic radius on tetravalent and trivalent cation diffusion rates in diopside is of the same order of magnitude as that observed in zircon [35,36]. In diopside, for example, the diffusion coefficient for Yb (0.985 Å radius in VIII-fold coordination [37]) is a factor of ~16 higher than for Ce (1.14 Å) at 1300°C. In zircon, the diffusion coefficient for Yb is a factor of ~19 higher than Sm (1.08 Å) at the same temperature. In contrast, ionic charge appears to be much less important in diopside than in zircon, particularly for the +3 and +4 ions. In diopside the diffusion coefficients for U^{4+} (1.00 Å) and Yb^{3+} (0.985 Å) differ by about an order of magnitude. In zircon the effect of ionic charge is much greater, with Yb diffusivity being about 5 orders of magnitude faster than U [35,36]. This difference may be a consequence of the relatively small energy of the divalent M2 lattice site in diopside compared to that of the tetravalent VIII-fold site in zircon.

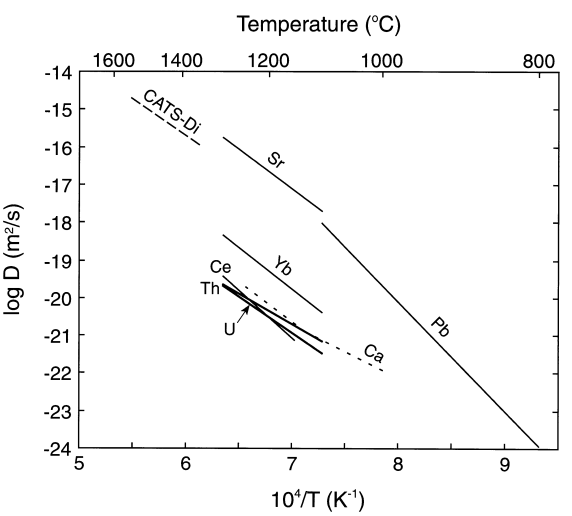

Fig. 5. Summary of cation diffusion data in natural, near end-member diopside. The dashed line labeled *CATS-Di* refers to interdiffusion of $CaAl_2SiO_6$ and diopside [30]. The dotted line shows Ca self-diffusion coefficients [31]. Solid lines refer to tracer diffusion coefficients for Sr [32], Pb [33], Yb and Ce [34], and U and Th (present study).

4.2. Early partial melting?

Several studies have observed that Fe-bearing pyroxenes exsolve a silica-enriched melt phase at temperatures far below their nominal melting temperatures [38,39]. This phenomenon, termed early partial melting (EPM), appears to be related to cation vacancies associated with Fe^{3+} impurities [40] and is sensitive to the Fe content of the pyroxene and the f_{O2} of the surrounding atmosphere. The diopside we used has less Fe (less than half by mole) than pyroxenes in which EPM has so far been observed, and it is unclear whether EPM would be expected under the conditions of our experiments. Optical inspection of our samples revealed no evidence for EPM, and if present, melt precipitates must be quite small in size. We note that where EPM has been unambiguously observed it has little effect on cation diffusion because the precipitates do not form an interconnected network. Dimanov et al. [31] observed abundant glassy precipitates under the optical microscope in their experiments on Ca self-diffusion in Fe-bearing diopside, yet observed only a very small (one might argue unresolvable) inflection in the Arrhenius curve at the onset of EPM. We consider EPM effects absent in our data.

5. Equilibration during melting and melt transport

In this section we use the U and Th diffusion data presented above to estimate the time scale of chemical equilibration during melting and melt transport. We first develop a scaling argument which shows that equilibrium between melt and the interiors of cpx grains is unlikely under most conditions appropriate to melting beneath mid-ocean ridges. We then use a numerical melting model to assess the degree of fractionation between U and Th during disequilibrium near-fractional melting.

5.1. Scaling argument

We follow the scaling approach adopted by Spiegelman and Kenyon [41] and Hart [42] to evaluate equilibration between clinopyroxene and melt during melt transport. The question we address is

whether partitioning of U and Th between clinopyroxene and melt will approach equilibrium under conditions relevant to the production and transport of mid-ocean ridge basalts.

For melt percolating upward through an upwelling porous matrix, diffusive equilibration is governed by the Peclet number, which is equal to the ratio of the characteristic time required for diffusive transport in the solid grains of the matrix to the time required for melt to move through the system. For melt flowing across a layer of thickness H, which for our purposes can be taken to be the height of the mantle melting column, the characteristic advection time can be written:

$$t_{adv} \approx \frac{H}{w} \tag{6}$$

where w is the melt velocity.

As discussed by Hart [42], the characteristic diffusion time, or more specifically the time required for the concentration of an element in the melt to reach 83% of its ultimate equilibrium value, is approximately:

$$t_D \approx \frac{r^2}{D(K)^{1.5}} \tag{7}$$

where r is the radius of a cylinder of melt, D is the diffusion coefficient in the solid, and K is the solid/melt equilibrium partition coefficient. In this expression, the characteristic diffusion time depends on the compatibility of the element being considered. An incompatible element ($K < 1$) requires longer diffusion times than a compatible element because a larger volume of solid must be tapped in order to provide its higher relative abundance in the melt.

In a grain-scale porous network with wetting angle ~50°, the radius of a melt tubule is related to the grain size d and porosity ϕ by [42,43]:

$$r \approx 0.13 d(\phi)^{1/2} \tag{8}$$

Conservation of mass in a one-dimensional upwelling column requires that [44]:

$$\phi = \frac{WF}{w} \tag{9}$$

where W is the solid velocity, w is the melt velocity, and F is the melting degree. Combining Eqs. 6–9, the Peclet number can be written:

$$\mathrm{Pe} = \frac{t_D}{t_{adv}} \approx \frac{d^2 WF}{59 D(K)^{1.5} H}. \tag{10}$$

For a Peclet number > 1, equilibration will be <83%.

Eq. 10 is equivalent to the expression derived by Hart [42] (his Eq. 6), who considered the time scale for growth of a melt tubule lying along grain boundaries rather than the time scale for porous flow through a network of melt tubules. These two time scales are the same because mass balance requires that the melt production and extraction rates are equal.

At 1400°C, a temperature relevant to melting beneath mid-ocean ridges [45–47], the diffusion coefficients for U and Th in clinopyroxene are both approximately 1.5×10^{-19} m^2/s, extrapolating from the Arrhenius relations given in Eqs. 3 and 4. Both U and Th have cpx/melt partition coefficients in the range 0.001–0.01 [9–13]. Taking a partition coefficient of 0.005, cpx grain diameter of 5 mm, mantle upwelling rate of 3 cm/yr, melting degree of 15%, and melting column height of 60 km, the Peclet number is ~20, which is within the disequilibrium domain. Fig. 6 explores a more complete range of parameter values and shows that partitioning of U and Th between clinopyroxene and melt will be a disequilibrium process except at very slow spreading ridges. For example, a 5 mm grain at peridotite solidus temperatures (~1400–1500°C) will approach

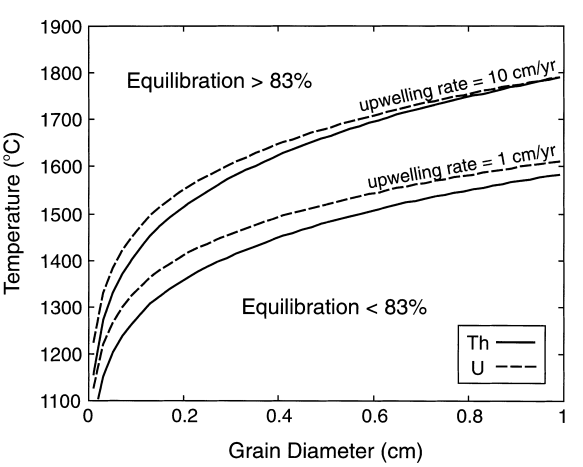

Fig. 6. Plot of cpx grain diameter vs. temperature showing the conditions under which U and Th partitioning equilibrium may be obtained during adiabatic melting. The curves represent solutions to Eq. 10, with $t_D/t_{adv} = 1$, for upwelling rates of 1 and 10 cm/yr. Each curve separates regions of greater than (above the curve) and less than 83% equilibration.

partitioning equilibrium only at upwelling rates of ~1 cm/yr or slower. In contrast to the usual assumption [3,7,42], we conclude that equilibrium may not be achieved during melting or grain-scale porous flow for highly incompatible and slowly-diffusing elements.

5.2. Numerical model

The scaling argument developed above allows us to estimate the conditions under which disequilibrium is expected during near-fractional melting, but it does not allow us to quantitatively predict the degree to which elements are fractionated due to their different diffusion rates. Numerical models have shown that the extent of elemental fractionation during disequilibrium melting is sensitive to the relative diffusion rates (e.g. [21–23]). We adopt the disequilibrium melting model of Qin [21], modified to allow for non-modal melting and for temperature-dependent (and therefore time-dependent) diffusion coefficients, in order to evaluate whether U and Th can be fractionated significantly by clinopyroxene, and in particular whether there are any conditions under which their compatibility order may be reversed.

The model we adopt is a near-fractional melting model modified to account for diffusion-controlled chemical equilibration between solid and its enclosing melt. The solid is assumed to be composed of spherical grains of equal size which retain their spherical symmetry during melting. These grains are assumed to be homogeneous in composition when melting begins, with ^{238}U and ^{230}Th in radioactive equilibrium. During melting, the interface between the solid and melt is always in chemical equilibrium, and concentrations in the interiors of grains are controlled by diffusion. Melt remains with the residue until a critical melt fraction is reached and is thereafter removed at the rate that keeps the porosity constant. Extracted melt is pooled in a chemically isolated reservoir, and both residual and extracted melts are assumed to homogenize continuously and instantaneously, an excellent approximation considering that U and Th diffusion in silicate melts is ~8 orders of magnitude faster than in clinopyroxene [48].

For simplicity, the melting rate is assumed to be constant, but clinopyroxene is allowed to dissolve at a rate different from that of the bulk rock, that rate depending on the stoichiometric coefficient for cpx in the melting reaction and on the abundance of cpx in the rock. We consider U and Th fluxes between clinopyroxene and melt only; in other words, we assume that when melting begins all of the U and Th in the system reside in cpx and that the solid/liquid partition coefficients for other solid phases are equal to zero.

The concentrations of ^{238}U and ^{230}Th in a cpx grain are expressed by:

$$\frac{\partial C^{\mathrm{U}}_{\mathrm{cpx}}}{\partial t} = D_{\mathrm{U}}(t)\left(\frac{\partial^2 C^{\mathrm{U}}_{\mathrm{cpx}}}{\partial r^2} + \frac{2}{r}\frac{\partial C^{\mathrm{U}}_{\mathrm{cpx}}}{\partial r}\right) - \lambda_{\mathrm{U}} C^{\mathrm{U}}_{\mathrm{cpx}}$$

$$\frac{\partial C^{\mathrm{Th}}_{\mathrm{cpx}}}{\partial t} = D_{\mathrm{Th}}(t)\left(\frac{\partial^2 C^{\mathrm{Th}}_{\mathrm{cpx}}}{\partial r^2} + \frac{2}{r}\frac{\partial C^{\mathrm{Th}}_{\mathrm{cpx}}}{\partial r}\right) - \lambda_{\mathrm{U}}\frac{m_{\mathrm{Th}}}{m_{\mathrm{U}}} C^{\mathrm{U}}_{\mathrm{cpx}} - \lambda_{\mathrm{Th}} C^{\mathrm{Th}}_{\mathrm{cpx}} \quad (11)$$

where $C^{\mathrm{U}}_{\mathrm{cpx}}$ and $C^{\mathrm{Th}}_{\mathrm{cpx}}$ are concentrations of ^{238}U and ^{230}Th at time t and radial distance r. λ_{U} and λ_{Th} are the decay constants and m_{U} and m_{Th} the masses of ^{238}U and ^{230}Th, respectively. These are expressions of Fick's second law in spherical coordinates, modified to account for decay of ^{238}U and ^{230}Th. The diffusion coefficients D_{U} and D_{Th} depend on the temperature-time path followed during melting and are thus functions of time. We assume that temperature decreases linearly with time and specify initial and final temperatures T_{i} and T_{f}.

Initial and boundary conditions for Eq. 11 are:

$$C^{\mathrm{U}}_{\mathrm{cpx}}(r,0) = C^{\mathrm{U}}_0$$
$$C^{\mathrm{Th}}_{\mathrm{cpx}}(r,0) = \frac{\lambda_{\mathrm{U}}}{\lambda_{\mathrm{Th}}} C^{\mathrm{U}}_0 \quad (12)$$

$$C^{\mathrm{U}}_{\mathrm{cpx}}(R(t),t) = K_{\mathrm{U}} C^{\mathrm{U}}_{\mathrm{m}}(t)$$
$$C^{\mathrm{Th}}_{\mathrm{cpx}}(R(t),t) = K_{\mathrm{Th}} C^{\mathrm{Th}}_{\mathrm{m}}(t) \quad (13)$$

where C^{U}_0 is the initial concentration of ^{238}U in the clinopyroxene and K_{U} and K_{Th} are the equilibrium cpx/melt partition coefficients for U and Th. The first pair of equations describes the initial condition, in which ^{238}U and ^{230}Th are assumed to be in radioactive equilibrium and distributed homogeneously in a grain of clinopyroxene. The second states that the clinopyroxene rim is at all times in equilibrium with the residual melt.

Concentrations in the residual melt are described by:

$$\frac{\mathrm{d}\left(V_\mathrm{m}C_\mathrm{m}^\mathrm{U}\right)}{\mathrm{d}t} = -4\pi R(t)^2\, D_\mathrm{U}(t)\frac{\partial C_\mathrm{cpx}^\mathrm{U}}{\partial r}\bigg|_{r=R(t)} + \upsilon_\mathrm{m}\gamma C_\mathrm{cpx}^\mathrm{U}(R(t),t) - \upsilon_\mathrm{e}C_\mathrm{m}^\mathrm{U} - \lambda_\mathrm{U}V_\mathrm{m}C_\mathrm{m}^\mathrm{U}$$

$$\frac{\mathrm{d}\left(V_\mathrm{m}C_\mathrm{m}^\mathrm{Th}\right)}{\mathrm{d}t} = -4\pi R(t)^2 D_\mathrm{Th}(t)\,\frac{\partial C_\mathrm{cpx}^\mathrm{Th}}{\partial r}\bigg|_{r=R(t)} + \upsilon_\mathrm{m}\gamma C_\mathrm{cpx}^\mathrm{Th}(R(t),t) - \upsilon_\mathrm{e}C_\mathrm{m}^\mathrm{Th} + V_\mathrm{m}\left(\lambda_\mathrm{U}\frac{m_\mathrm{Th}}{m_\mathrm{U}}C_\mathrm{m}^\mathrm{U} - \lambda_\mathrm{Th}C_\mathrm{m}^\mathrm{Th}\right) \quad (14)$$

where C_m^U and C_m^Th are concentrations in the residual melt, V_m is the volume of residual melt, $R(t)$ is the radius of a clinopyroxene grain, υ_m and υ_e are the volumetric melting and melt extraction rates, respectively, and γ is the stoichiometric coefficient of clinopyroxene in the melting reaction. The terms on the right-hand side of Eq. 14 represent, in order, (1) the total diffusive current across the cpx/melt interface at time t, (2) the U or Th mass flux out of the clinopyroxene by melting, (3) the mass flux out of the system by melt extraction, and (4) changes in mass due to decay of ^{238}U and ^{230}Th.

In the pooled extracted melt, concentrations are given by:

$$\frac{\mathrm{d}\left(V_\mathrm{M}C_\mathrm{M}^\mathrm{U}\right)}{\mathrm{d}t} = \upsilon_\mathrm{e}C_\mathrm{m}^\mathrm{U} - \lambda_\mathrm{U}V_\mathrm{M}C_\mathrm{M}^\mathrm{U}$$

$$\frac{\mathrm{d}\left(V_\mathrm{M}C_\mathrm{M}^\mathrm{Th}\right)}{\mathrm{d}t} = \upsilon_\mathrm{e}C_\mathrm{m}^\mathrm{Th} + V_\mathrm{M}\left(\lambda_\mathrm{U}\frac{m_\mathrm{Th}}{m_\mathrm{U}}C_\mathrm{M}^\mathrm{U} - \lambda_\mathrm{Th}C_\mathrm{M}^\mathrm{Th}\right) \quad (15)$$

where C_M^U and C_M^Th are concentrations in the extracted melt and V_M is the volume of melt extracted.

The melting rate, υ_m, is taken to be constant and is equal to:

$$\upsilon_\mathrm{m} = \frac{V_0 W F}{H} \quad (16)$$

where W is the solid upwelling velocity, F is the total degree of melting, and H is the height of the melting column. V_0 is the initial solid volume, defined as $V_0 = 4/3\pi R_0^3/X_\mathrm{cpx}$, where X_cpx is the volume fraction of clinopyroxene in the solid. The melt extraction rate, υ_e, is initially zero and is equal to:

$$\upsilon_\mathrm{e} = \frac{1}{1-\phi_\mathrm{crit}}\upsilon_\mathrm{m} \quad (17)$$

when the melt fraction exceeds the critical value, ϕ_crit. The radius of a clinopyroxene grain, $R(t)$, changes with time according to:

$$R(t) = R_0\left(1 - \frac{\upsilon_\mathrm{m}\gamma t}{V_0 X_\mathrm{cpx}}\right). \quad (18)$$

Eqs. 11–18 were solved numerically using an implicit Crank–Nicolson finite difference scheme. The moving boundary between clinopyroxene and melt was accommodated by keeping a fixed number of radial grid points and rescaling the grid to the new grain radius at each time step.

We performed a series of model runs using the parameter values listed in Table 3. In each, the radial distribution of ^{238}U and ^{230}Th in cpx spheres and their concentrations in the residual and aggregated melts are calculated as functions of time. Fig. 7a illustrates the evolution of Th and U distributions in a cpx sphere under melting conditions typical for fast spreading ridges. Note that the interior of the crystal maintains high relative concentrations of U and Th and is far from equilibrium with the residual melt even at high degrees of melting. In contrast, at slow spreading ridges (Fig. 7b) clinopyroxene crystals approach equilibrium with the residual liquid. The upwelling rate at which disequilibrium becomes important depends on several factors, most importantly

Table 3
Model parameters and values

Parameter	Value(s)
ϕ, critical melt fraction	0.001–0.01
K_U, U cpx/liq partition coefficient	0.005
K_Th, Th cpx/liq partition coefficient	0.01
γ, cpx coefficient in melting reaction	0.80
X_cpx, volume fraction cpx	0.15
R_0, cpx initial radius, mm	1–5
H, melting column height, km	33–63
F, melting degree	0.10–0.20
W, mantle upwelling rate, cm/yr	1–10
T_i, initial temperature, K	1588–1748
T_f, final temperature, K	1506–1514

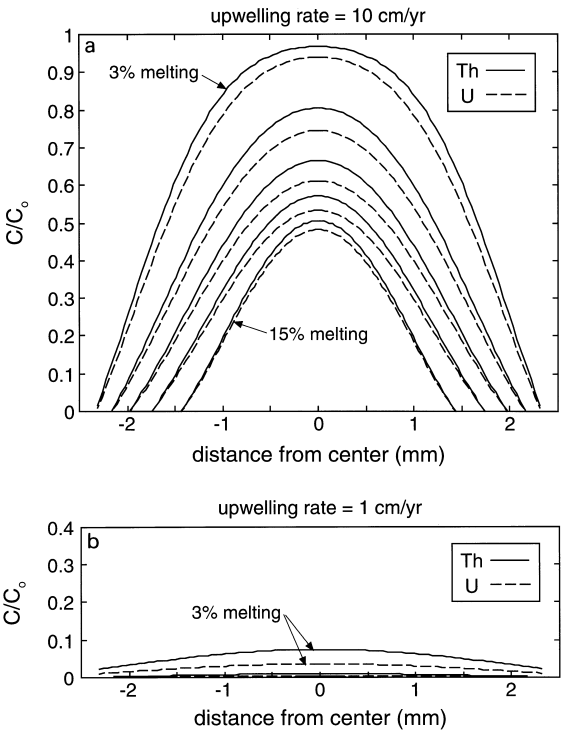

Fig. 7. Model Th and U diffusion profiles developed across a 2.5 mm clinopyroxene grain during progressive melting. (a) For a mantle upwelling rate of 10 cm/yr cpx is in strong disequilibrium with the melt, even after 15% melting. (b) In contrast, at 1 cm/yr cpx is near equilibrium with the melt after only ~3% melting. Both figures show elemental rather than isotopic concentrations. $\phi = 1\%$, $T_i = 1395$°C, $T_f = 1240$°C, $H = 48$ km.

the grain size. The examples shown in Fig. 7 both used an initial grain diameter of 5 mm. This is within the range of cpx grain sizes (~2–10 mm diameter) in fertile peridotite xenoliths from Pali-Aike, Chile, which geochemically and isotopically resemble unmelted MORB-source mantle [49]. Clinopyroxene grains from abyssal peridotites are typically smaller, with diameters up to 2–3 mm [50,51], but these rocks represent melting residues and are more appropriate for estimating the final, rather than initial, cpx radii. The actual size of cpx grains in unmelted MORB mantle is not well known, but a range of 2–10 mm provides a realistic lower limit. In model runs using an initial cpx diameter of 2 mm (not shown), cpx is in moderate disequilibrium with residual melt for fast spreading ridges (upwelling rate of 10 cm/yr). For an initial diameter of 10 mm, strong disequilibrium develops even at upwelling rates as slow as 1 cm/yr.

5.3. Deformation of high-Ca pyroxene during mantle upwelling

It is reasonable to question whether the model presented above is realistic for describing a solid mantle that deforms as it ascends. The model considers spherical high-Ca pyroxene grains that remain undeformed during decompression melting. Deformation of these grains would decrease the net diffusion length, thereby increasing the degree of equilibration between solid and melt. It is therefore important to assess the degree of deformation that is expected beneath mid-ocean ridges.

The degree to which high-Ca pyroxene is deformed during upwelling depends on its viscosity relative to the viscosities of olivine and orthopyroxene. Plastic flow laws of the form

$$\dot{\varepsilon} = \dot{\varepsilon}_0 (f_{O_2})^m \sigma^n \exp(-Q/RT), \tag{19}$$

where $\dot{\varepsilon}$ is strain rate and σ shear stress, have been determined for olivine [52], orthopyroxene [53], and diopside [54] and are given in Table 4. Under typical upper mantle conditions of $T = 1400$°C, $f_{O2} = 4 \times 10^{-7}$ atm, and $\sigma = 30$ MPa, the viscosities of olivine and orthopyroxene are, respectively, 2.6×10^{12} and 7.4×10^{13} Pa s. Diopside, in contrast, is several orders of magnitude stiffer than either of these minerals, having a viscosity of 1.9×10^{17} Pa s under the same conditions. We therefore expect that olivine and orthopyroxene will accommodate most of the strain associated with upwelling and that high-Ca pyroxene will remain relatively undeformed. The assumption in our model that high-Ca pyroxene grains remain undeformed therefore seems reasonable.

5.4. Implications for $^{238}U/^{230}Th$ radioactive disequilibrium in MORB

It is clear that under certain melting conditions solid-state diffusion may exert strong control on the fluxes of U and Th between cpx and melt. Can excess ^{230}Th in the melt be generated under these conditions? Fig. 8a shows activity ratios [^{230}Th/^{238}U] in the aggregated melt for a model run with cpx

Table 4
Flow laws for olivine, orthopyroxene, and diopside

Mineral	Orientation of stress axis	ε_0 (σ in MPa)	n	m	Q (kJ/mol)	ε [a]	Ref.	Comments
Olivine (Fo_{91})	[110]	0.02	3.5	0.36	230	ε_1	[52]	buffered by opx
		1.3×10^{22}	3.5	0.10	1000	ε_2	[52]	
		1.2	3.5	0.15	290	ε_3	[52]	
Orthopyroxene (En_{96})	random	2.1×10^{15}	3.9	0	880		[53]	buffered by olivine
Diopside	[110]	7.0×10^{-18}	6.0	0	48		[54]	for $T > 1130$°C

[a] For olivine, $\varepsilon = \varepsilon_1 + [\varepsilon_2^{-1} + \varepsilon_3^{-1}]^{-1}$.

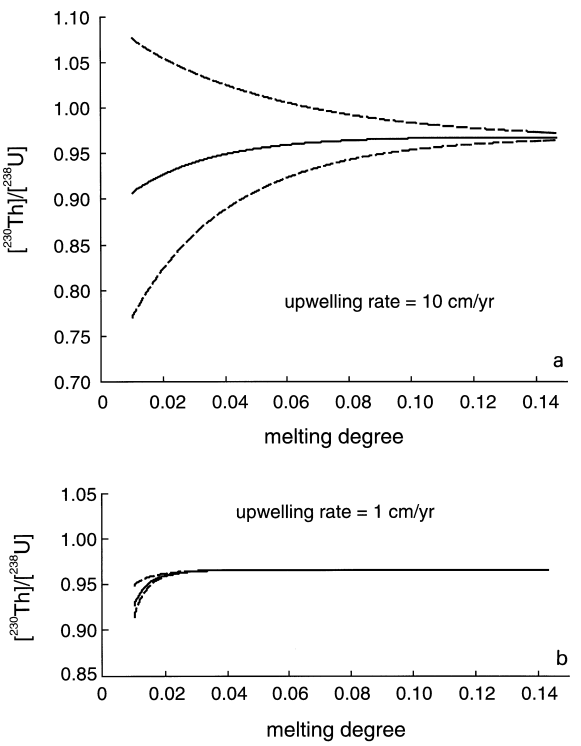

Fig. 8. $[^{230}Th/^{238}U]$ activity ratios in the aggregated melt. The dashed curves define an uncertainty envelope that is based on the error in the Arrhenius parameters for U and Th. Uranium and thorium are not efficiently fractionated under either (a) disequilibrium or (b) near-equilibrium melting conditions, and in both cases the activity ratio is near 1 throughout most of the melting interval. Parameter values are the same as those used in the calculations shown in Fig. 7.

diameter of 5 mm and upwelling rate of 10 cm/yr. The solid curve was generated using the Arrhenius relations for U and Th given in Eqs. 3 and 4. The activity ratio is always below 1 and gradually converges on a steady-state value of ~0.97 as melting progresses. ^{230}Th excesses never occur because during the early stages of melting, at high temperature, U has a higher diffusivity than Th and is thus released more quickly into the melt. The dashed curves reflect the uncertainty in the relative diffusivity of U and Th, and were generated by running the model with U and Th Arrhenius lines rotated within their 1σ uncertainty limits. The upper curve pairs the steepest Th Arrhenius line with the shallowest U Arrhenius line, and the lower curve vice versa. The uncertainty envelope covers a moderate range of activity ratios at small melting degrees, including a region of small ^{230}Th excesses, but at higher degrees of melting becomes quite narrow and does not overlap the region with $[^{230}Th/^{238}U] > 1$.

Fig. 8b shows a similar plot for an upwelling rate of 1 cm/yr. In this case cpx is close to equilibrium with the melt, and varying the U and Th Arrhenius parameters within their uncertainty limits has little effect on the activity curves. The activity ratio has a nearly constant value of ~0.96 for melting degrees above ~2%.

We conclude that it is highly unlikely that high-Ca pyroxene could be responsible for generating the ^{230}Th excesses observed in MORB. Most MORB lavas have $[^{230}Th/^{238}U]$ activity ratios of 1.1–1.4 (e.g. [14,15]), well outside the uncertainty limits defined by the upper and lower curves in Fig. 8a or b. Even at a very high degree of chemical disequilibrium, with a cpx diameter of 10 mm and an upwelling rate of 10 cm/yr, the uncertainty envelope never extends to an activity ratio above 1.15. Clinopyroxene can therefore be ruled out as the source of the ^{230}Th excess signal observed in ocean floor basalts, as it is unable to produce significant ^{230}Th excesses under either equilibrium or disequilibrium conditions.

Acknowledgements

We thank George Harlow for providing the diopside specimens used in this study; Graham Layne for keeping the ion probe in top working order and for very helpful suggestions on depth profiling techniques; and Daniele Cherniak, John Longhi and Tom LaTourrette for insightful and thorough reviews of the manuscript. This work was supported by an NSF Graduate Fellowship and by NSF OCE-9415968. ***[CL]***

References

[1] D. McKenzie, ^{230}Th–^{238}U disequilibrium and the melting process beneath ridge axes, Earth Planet. Sci. Lett. 72 (1985) 149–157.

[2] R.W. Williams, J.B. Gill, Effects of partial melting on the uranium decay series, Geochim. Cosmochim. Acta 53 (1989) 1607–1619.

[3] M. Spiegelman, T. Elliott, Consequences of melt transport for uranium series disequilibrium in young lavas, Earth Planet. Sci. Lett. 118 (1993) 1–20.

[4] Z. Qin, Dynamics of melt generation beneath mid-ocean ridge axes: Theoretical analysis based on ^{238}U–^{230}Th–^{226}Ra and ^{235}U–^{231}Pa disequilibria, Geochim. Cosmochim. Acta 57 (1993) 1629–1634.

[5] H. Iwamori, ^{238}U–^{230}Th–^{226}Ra and ^{235}U–^{231}Pa disequilibria produced by mantle melting with porous and channel flows, Earth Planet. Sci. Lett. 125 (1994) 1–16.

[6] C. Richardson, D. McKenzie, Radioactive disequilibria from 2D models of melt generation by plumes and ridges, Earth Planet. Sci. Lett. 128 (1994) 425–437.

[7] C.C. Lundstrom, J. Gill, Q. Williams, M.R. Perfit, Mantle melting and basalt extraction by equilibrium porous flow, Science 270 (1995) 1958–1961.

[8] T. Elliott, Fractionation of U and Th during mantle melting: a reprise, Chem. Geol. 139 (1997) 165–183.

[9] T.Z. LaTourrette, D.S. Burnett, Experimental determination of U and Th partitioning between clinopyroxene and natural and synthetic basaltic liquid, Earth Planet. Sci. Lett. 110 (1992) 227–244.

[10] P. Beattie, The generation of uranium series disequilibria by partial melting of spinel peridotite: constraints from partitioning studies, Earth Planet. Sci. Lett. 117 (1993) 379–391.

[11] E.H. Hauri, T.P. Wagner, T.L. Grove, Experimental and natural partitioning of Th, U, Pb, and other trace elements between garnet, clinopyroxene, and basaltic melts, Chem. Geol. 117 (1994) 149–166.

[12] C.C. Lundstrom, H.F. Shaw, F.J. Ryerson, D.L. Phinney, J.B. Gill, Q. Williams, Compositional controls on the partitioning of U, Th, Ba, Pb, Sr, and Zr between clinopyroxene and haplobasaltic melts: implications for uranium series disequilibria in basalts, Earth Planet. Sci. Lett. 128 (1994) 407–423.

[13] V.J.M. Salters, J. Longhi, Partitioning of trace elements during primary melting of MORB mantle, J. Conf. Abstr. 1 (1996) 529.

[14] M. Condomines, Ch. Hemond, C.J. Allegre, U–Th–Ra radioactive disequilibria and magmatic processes, Earth Planet. Sci. Lett. 90 (1988) 243–262.

[15] B. Bourdon, A. Zindler, T. Elliott, C.H. Langmuir, Constraints on mantle melting at mid-ocean ridges from global ^{238}U–^{230}Th disequilibrium data, Nature 385 (1996) 231–235.

[16] P. Beattie, Uranium–thorium disequilibria and partitioning on melting of garnet peridotite, Nature 363 (1993) 63–65.

[17] T.Z. LaTourrette, A.K. Kennedy, G.J. Wasserburg, Thorium–uranium fractionation by garnet: evidence for a deep source and rapid rise of oceanic basalts, Science 261 (1993) 739–742.

[18] E. Takahashi, I. Kushiro, Melting of a dry peridotite at high pressures and basalt magma genesis, Am. Mineral. 68 (1983) 859–879.

[19] E. Takahashi, Melting of a dry peridotite KLB-1 up to 14 GPa: implication on the origin of peridotitic upper mantle, J. Geophys. Res. 91 (1986) 9367–9382.

[20] M.M. Hirschmann, E.M. Stolper, A possible role for garnet pyroxenite in the origin of the 'garnet signature' in MORB, Contrib. Mineral. Petrol. 124 (1996) 185–208.

[21] Z. Qin, Disequilibrium partial melting model and its implications for trace element fractionations during mantle melting, Earth Planet. Sci. Lett. 112 (1992) 75–90.

[22] H. Iwamori, Dynamic disequilibrium melting model with porous flow and diffusion controlled chemical equilibration, Earth Planet. Sci. Lett. 114 (1993) 301–313.

[23] H. Iwamori, A model for disequilibrium mantle melting incorporating melt transport by porous and channel flows, Nature 366 (1993) 734–737.

[24] E.M. Levin, C.R. Robbins, H.F. McMurdie, Phase Diagrams for Ceramists, 601 pp., The American Ceramic Society, Columbus, OH, 1964.

[25] A.T. Chapman, R.E. Meadows, Volatility of $UO_{2\pm x}$ and phase relations in the system uranium–oxygen, J. Am. Ceram. Soc. 47 (1964) 614–621.

[26] J. Crank, The Mathematics of Diffusion, 2nd ed., Oxford Univ. Press, Oxford, 1975, 414 pp.

[27] P.R. Bevington and D.K. Robinson, Data Reduction and Error Analysis for the Physical Sciences, 2nd ed., McGraw-Hill, New York, 1992, 328 pp.

[28] D. York, Least squares fitting of a straight line with correlated errors, Earth Planet. Sci. Lett. 3 (1969) 320–324.

[29] M.G. Seitz, Uranium and thorium diffusion in diopside and fluorapatite, Carnegie Inst. Washington Yearb. 72 (1973) 586–588.

[30] T.L. Grove, T.P. Wagner, Is adiabatic melting of oceanic mantle a disequilibrium process? Constraints from experimental measurement of element diffusion rates in high-Ca pyroxene, Eos Trans. AGU 74 (1993) 284.

[31] A. Dimanov, O. Jaoul, V. Sautter, Calcium self-diffusion

in natural diopside single crystals, Geochim. Cosmochim. Acta 60 (1996) 4095–4106.
[32] M. Sneeringer, S.R. Hart, N. Shimizu, Strontium and samarium diffusion in diopside, Geochim. Cosmochim. Acta 48 (1984) 1589–1608.
[33] D.J. Cherniak, Pb diffusion in pyroxene, Eos Trans. AGU 78 (1997) S336.
[34] J.A. Van Orman, N. Shimizu, T.L. Grove, Diffusion of Ce and Yb in diopside: Disequilibrium effects on rare earth element patterns in high-Ca pyroxenes in abyssal peridotites, Eos Trans. AGU 78 (1997) F836.
[35] D.J. Cherniak, J.M. Hanchar, E.B. Watson, Rare-earth diffusion in zircon, Chem. Geol. 134 (1997) 289–301.
[36] D.J. Cherniak, J.M. Hanchar, E.B. Watson, Diffusion of tetravalent cations in zircon, Contrib. Mineral. Petrol. 127 (1997) 383–390.
[37] R.D. Shannon, Revised effective ionic radii and systematic studies of interatomic distances in halides and chalcogenides, Acta Crystall. A32 (1976) 751–767.
[38] J. Ingrin, N. Doukhan, J.C. Doukhan, High temperature deformation of diopside single crystal: 2. TEM investigation of the defect microstructures, J. Geophys. Res. 96 (1991) 14287–14297.
[39] N. Doukhan, J.C. Doukhan, J. Ingrin, O. Jaoul, P. Raterron, Early partial melting in pyroxenes, Am. Mineral. 78 (1993) 1247–1257.
[40] O. Jaoul, P. Raterron, High-temperature deformation of diopside crystal: 3. Influence of pO_2 and SiO_2 precipitation, J. Geophys. Res. 99 (1994) 9423–9439.
[41] M. Spiegelman, P. Kenyon, The requirements for chemical disequilibrium during magma migration, Earth Planet. Sci. Lett. 109 (1992) 611–620.
[42] S.R. Hart, Equilibration during mantle melting: A fractal tree model, Proc. Natl. Acad. Sci. 90 (1993) 11914–11918.
[43] N. von Bargen, H.S. Waff, Permeabilities, interfacial areas, and curvatures of partially molten systems: results of numerical computations of equilibrium microstructures, J. Geophys. Res. 91 (1986) 9261–9276.
[44] M. Spiegelman, Physics of melt extraction: theory, implications, and applications, Philos. Trans. R. Soc. London A 342 (1993) 23–41.
[45] E.M. Klein, C.H. Langmuir, Global correlations of ocean ridge basalt chemistry with axial depth and crustal thickness, J. Geophys. Res. 92 (1987) 8089–8115.
[46] D. McKenzie, M.J. Bickle, The volume and composition of melt generated by extension of the lithosphere, J. Petrol. 29 (1988) 625–679.
[47] R.J. Kinzler, T.L. Grove, Primary magmas of mid-ocean ridge basalts, 2. Applications, J. Geophys. Res. 97 (1992) 6907–6926.
[48] T. LaTourrette, G.J. Wasserburg, Self diffusion of europium, neodymium, thorium, and uranium in haplobasaltic melt: The effect of oxygen fugacity and the relationship to melt structure, Geochim. Cosmochim. Acta 61 (1997) 755–764.
[49] C.R. Stern, S. Saul, M.A. Skewes, K. Futa, Garnet peridotite xenoliths from the Pali-Aike alkali basalts of southernmost South America, Geol. Soc. Aust. Spec. Pub. 14 (1989) 735–744.
[50] S.C. Komor, T.L. Grove, R. Hebert, Abyssal peridotites from ODP Hole 670A (21°10′N, 45°02′W): Residues of mantle melting exposed by non-constructive axial divergence, in: R. Detrick, J. Honnorez, W.B. Bryan, T. Juteau et al. (Eds.), Proc. ODP, Sci. Results 106/109 (1990) 85–99.
[51] H.J.B. Dick, J.H. Natland, Late-stage melt evolution and transport in the shallow mantle beneath the East Pacific Rise, in: C. Mevel, K.M. Gillis, J.F. Allan, P.S. Meyer (Eds.), , Proc. ODP, Sci. Results 147 (1996) 103–134.
[52] Q. Bai, S.J. Mackwell, D.L. Kohlstedt, High-temperature creep of olivine single crystals, 1. Mechanical results for buffered samples, J. Geophys. Res. 96 (1991) 2441–2463.
[53] S.J. Mackwell, High-temperature rheology of enstatite: implications for creep in the mantle, Geophys. Res. Lett. 18 (1991) 2027–2030.
[54] P. Raterron, O. Jaoul, High-temperature deformation of diopside single-crystal, 1. Mechanical data, J. Geophys. Res. 96 (1991) 14277–14286.